ISIJ International, Vol. 59 (2019), No. 10, pp. 1846–1852

Applicability of Time-Gated Raman Spectroscopy in the Characterisation of Calcium-Aluminate Inclusions

Francis GYAKWAA,[1)]* Matti AULA,[1)] Tuomas ALATARVAS,[1)] Tero VUOLIO,[1)] Marko HUTTULA[2)] and Timo FABRITIUS[1)]

1) Process Metallurgy Research Unit, University of Oulu, P.O. Box 4300, FI–90014, University of Oulu, Finland.
2) Nano and Molecular Systems Research Unit, University of Oulu, P.O. Box 4300, FI–90014, University of Oulu, Finland.

(*Received on February 26, 2019; accepted on May 10, 2019; J-STAGE Advance published date: July 23, 2019*)

Calcium aluminate ($CaO–Al_2O_3$) phases play a critical role in the study of non-metallic inclusions in aluminium killed, and calcium treated steels. In this study, the Raman spectroscopy technique, a versatile and non-destructive approach, was used to characterise binary calcium aluminate phases qualitatively and quantitatively. Calcium aluminate samples with varying CaO/Al_2O_3 ratios were synthesised to produce a binary phase samples mixture of C12A7–C3A and C12A7–CA. Quantitative estimation was based on plotting a linear regression calibration model between the ratio of Raman band intensities and the phase fraction in the samples. With the linear regression, the phase fraction of C12A7–C3A and C12A7–CA was estimated with average absolute errors of 2.97 and 2.55 percentage points. This work demonstrates the potential suitability of using Raman spectroscopy technique for evaluating whether calcium aluminate phases in oxide inclusions fall within the liquidus region at steelmaking temperatures.

KEY WORDS: Raman spectroscopy; non-metallic inclusion; calcium aluminate; liquidus region.

1. Introduction

The formation, modification and impact of non-metallic inclusions are essential factors in assessing steel cleanliness and quality. Non-metallic inclusions such as sulphides, nitrides, and oxides may be detrimental to steel production and its properties. For instance, fatigue failure, degradation of surface quality and submerged entry nozzle (SEN) clogging are attributed to inclusions making it necessary for these inclusions to be removed or modified.[1–3)] In steelmaking processes, a high oxygen content is undesirable and should be controlled or monitored. A deoxidation process is used to reduce the total oxygen content[3,4)] by introducing aluminium into the molten steel.[5,6)] However, Al-killed steels process control encounter the challenges associated with the formation of solid alumina and aluminate inclusions from the deoxidation process.[7)] The prevention of submerged entry nozzle clogging can be achieved if the inclusions are liquid during the continuous casting process. Calcium treatment is used in aluminium-killed steel with the aim of generating calcium aluminate inclusions with a low liquidus temperature, such as $12CaO.7Al_2O_3$ (C12A7).[8–12)] The amount of calcium-containing wire, such as CaSi added during calcium treatment, needs to be in the correct range. The excess addition of Ca in the presence of sulfur in the molten steel may form CaS, while adding too little Ca may lead to incomplete modification of alumina inclusions, which in turn generates solid calcium aluminates, which have high melting temperatures.[8,13)]

Various techniques for steel cleanliness assessment and quality control for non-metallic inclusion characterisation have been studied. Examples of these include scanning electron microscopy (SEM),[12,14,15)] metallographic microscope observation (MMO),[12)] energy-dispersive X-ray microanalysis (EDX),[10)] cathodoluminescence analysis[16,17)] and some other more specific methods classified by other authors.[3,18,19)] Raman spectroscopy is a promising method to study non-metallic inclusions of calcium aluminate ($CaO–Al_2O_3$). The use of Raman spectroscopy has some advantages over conventional inclusion characterization and assessment methods such as rapid analysis, relatively easy sample preparation, non-destructive sample measurements and the ability to identify the chemical composition of phases relevant to steelmaking. Raman spectroscopy techniques have been demonstrated as a potential tool for both the qualitative and quantitative characterisation for Raman active samples.[20–24)] Furthermore, steel is not Raman active, which means that the Raman spectra measured from steel samples originate from the inclusions in the steel. Previous studies have used Raman spectroscopy to distinguish different calcium aluminate phases[25–29)] and for specific inclusions characterisations.[30–32)] The previous works have mainly focused on the characterisation of individual phases, but binary calcium aluminate phases have not been quantified. Multiphase analysis for studying oxide inclusions is relevant in steelmaking, since inclusions may generally occur as a mixture of phases. Additionally, multiphase research will

* Corresponding author: E-mail: Francis.gyakwaa@oulu.fi
DOI: https://doi.org/10.2355/isijinternational.ISIJINT-2019-122

provide significant information to estimate the liquidus boundary for binary $CaO–Al_2O_3$ towards achieving liquid oxide inclusions.

The aim of this work is to study the applicability of Raman spectroscopy in the characterisation of binary phases of monocalcium aluminate, $CaO·Al_2O_3$ (CA), mayenite $12CaO·7Al_2O_3$ (C12A7), and tricalcium aluminate, $3CaO·Al_2O_3$ (C3A). In addition, the suitability of the method to find an indication of liquid calcium aluminate inclusions relevant to steelmaking will be evaluated.

2. Experimental

2.1. Preparation of the Samples

The calcium aluminate samples were prepared from aluminum oxide and calcium oxide obtained from Alfa Aesar (purity in the range of 99.7% to 99.9%), by varying the CaO/Al_2O_3 (C/A) ratio ranging from 1.0 to 3.0 to achieve binary phase mixtures of interest (C12A7–CA and C12A7–C3A). The samples were pressed into pellets, placed in a crucible and sintered at a high temperature of 1 350°C in a chamber furnace. The phase fraction of C12A7 was varied between 20% to 80% in each binary phase samples of C12A7–C3A and C12A7–CA prepared. Before XRD, XRF and Raman measurements, the pellets were milled into the form of a powder.

2.2. Sample Characterisation

The calcium aluminate phases in the samples were identified, and the phase fraction was measured using XRD. The XRD of consisted of a Cu source lamp with 45 kV and 200 mA settings (9 kW rotating anode). It was equipped with Bragg-Brentano para-focusing geometry (300 mm goniometer), with a speed of acquisition of 3 degrees/minute at 0.02 degrees/step. A 10 mm length limiting slit was used on the source side for the samples in standard glass holders with 5 degree Soller slits used on both sources, and on the analyser side (a 0.5 degree incident slit is used to limit beam divergence). As the XRD gives only a semi-quantitative measure of the phase fractions, an XRF analysis was conducted to verify the chemical compositions of the samples. The XRF used for elemental sample analysis was an Axios Max model from Panalytical. It uses SuperQ as its analysis software, with X-ray generator Rh-tube, and a maximum power of 4 kW.

2.3. Time-gated Raman Spectroscopy

Raman spectroscopy is a spectroscopic technique that uses the inelastic scattering of monochromatic light to study the vibrational and rotational modes of excited molecules of a material.[33] The laser beams interaction with the molecular vibration in the material causes a change in the energy of the scattered photons. The characterisation of the material results from the change in energy that is a characteristic function of the vibrational modes of the molecule. This makes it possible to identify a specific substance from the Raman spectrum measured from that substance as a fingerprint.

The application of Raman spectroscopy as an analytical technique is found in some research areas in steelmaking such as for slag structure and viscosities studies.[24,34–41] The use of Raman spectroscopy has some advantages over other similar methods. The main advantages are because it is a non-destructive technique, it requires low sample volumes and it has a relatively fast detection speed. However, there are some potential sources of errors with the use of Raman spectroscopy, and these include: instrumental effects such as the sensitivity of the detector; misalignment in the optical system; and the impact of fluorescence in the Raman spectra. Recent Raman spectroscopy technologies seek to address these challenges. TimeGated® Raman spectroscopy is an example of such an improvement in handling the effect of fluorescence. TimeGated® Raman technology has an advantage compared to the Achilles' heel of conventional Raman technology since it can be used to achieve real fluorescence rejection and helps prevent other photoluminescence phenomena that may interfere or overlap with the Raman signals making the sample identification challenging.[42] A TimeGated® 532 Raman spectrometer (TG532 M1) from TimeGated instruments Ltd, was used for acquiring the Raman spectra from the samples. The TimeGated® Raman spectrometer (TG532 M1) utilises a fibre-coupled and pulsed laser of 532 nm and a shot length of 150 ps with a frequency range from 40 to 100 kHz. The spectral width of the laser was less than 0.1 nm and the power varies from 30 to 60 mW. The probe head was a Photonics RPB532 w/105 μm excitation fibre and a 200 μm collection fibre with a spot size of 1 mm. The spectrometer component consisted of a fibre-coupled spectrograph, CMOS-SPAD array detector, delay electronics with an auxiliary and other electronics and mechanics. A Raman spectra range of 100–1 200 cm^{-1} with a resolution of 10 cm^{-1} and an acquisition time of 3–5 minutes were used for the sample measurements. A rotating sample stage was used during the measurements to obtain spatially averaged spectra.

2.4. Calibration Model Identification

The connections between different Raman peak ratios and phase fractions were analysed with a calibration model. The calibration features to predict the variance in the phase fractions based on the summed Raman spectrum were defined as the relative intensities of the observed intensity peaks in the spectrum. The calibration feature candidate can be expressed as:

$$x_c = \frac{I_k}{(I_n + I_k)}, \quad \text{..... (1)}$$

where x_c is the calibration feature candidate, I_k is the intensity corresponding to the Raman shift k and I_n is the intensity corresponding to the Raman shift n.

Before the analysis, zero means and unit variance normalisation were applied to the data. The normalised relative intensities of the peaks identified from the summed Raman spectra were transformed into phase fractions with a simple linear regression calibration model. The error function for the calibration parameters can be given:[43]

$$\min \sum_{i=1}^{k} \left(y_{i,t.} - \hat{y}_{i,t.} \right)^2 = \min \sum_{i=1}^{k} \left(y_{i,t.} - \left[b_1 \frac{I_{k,t.}}{(I_{n,t.} + I_{k,t.})} + b_0 \right] \right)^2, \quad \text{..... (2)}$$

where t means the training subset. The least-squares solution

of the error function is given by Moore-Penrose inversion:[43)]

$$\hat{b} = (X^T X)^{-1} X^T y, \quad \text{..... (3)}$$

where X is the data matrix. The evaluation of the calibration variables was carried out with a manual feature selection technique combined with the Leave-Multiple-Out cross-validation procedure, which is introduced in more detail in.[44,45)] For cross-validation, the data was split so that 80% was used for training and 20% for external validation of the models. The prediction performance and the distribution of the calibration parameters were approximated by repeating the cross-validation 4*N* times. According to Baumann *et al*.[45)] The Leave-Multiple-Out cross-validation prevents a chance correlation efficiently and leads to more stable models.[45)] The final selection was made by selecting the relative intensity and a model parameter distribution that minimises the average mean absolute error for training and validation sets for 4*N* repetitions. This being so, the objective function for the final calibration model selection is given by:

$$\min \frac{1}{4N} \sum_{l=1}^{4N} MAE_{l,t.} + MAE_{l,cv}, \quad \text{..... (4)}$$

where N is the number of data points in the training set, k is the number of data points in the validation set and l is the split repetition. The MAE is defined as:

$$\text{MAE} = \frac{1}{k} \sum_{i=1}^{k} \left| y_{i,t.} - \hat{y}_{i,t.} \right|. \quad \text{..... (5)}$$

The stability of the calibration feature candidates was analysed with the ratio of mean and standard deviation of a normalised regression coefficient between the split repetitions, which is given as follows:

$$s_i = \frac{\frac{1}{4N} \sum_{j=1}^{4N} b_{i,j}}{\sqrt{\frac{1}{4N} \sum_{j=1}^{4N} (b_{i,j} - \bar{b}_{i,j})^2}}, \quad \text{..... (6)}$$

where $b_{i,j}$ is the identified regression coefficient for training subset j and variable i.

3. Results and Discussion

3.1. Reference Data

Figure 1 shows an example of XRD spectra for binary samples containing C12A7 and C3A, where *A*, *B* and *C* represent 20%, 40% and 80% phase fractions of C12A7 in each sample. Similarly, **Fig. 2** illustrates *A*, *B* and *C* corresponding to 20%, 40% and 80% phase fractions of C12A7 for C12A7–CA binary samples. XRF was used for elemental analysis to determine the weight percentages of CaO and Al_2O_3 in the samples already studied with XRD. **Tables 1** and **2** show a comparison of the weight percentages of CaO and Al_2O_3 between the XRD calculated and XRF measured values. A systematic difference was noticed between XRD and XRF associated with the weight percentage for CaO and Al_2O_3. For C12A7–C3A binary phase samples had an average difference and standard deviation of 2.92 wt% and 0.52 wt%, respectively.

Similarly, the C12A7–CA sample had an estimated average difference of 3.38 wt% and a standard deviation of 0.61 wt%. Even though there is a systematic difference between the reference methods for both of the binary systems, the standard deviations of the differences are relatively small. Since for a binary phase sample such as CaO–Al_2O_3 it is straightforward to evaluate the phase fractions, the phase fractions from the XRD analysis were selected for further quantitative analysis.

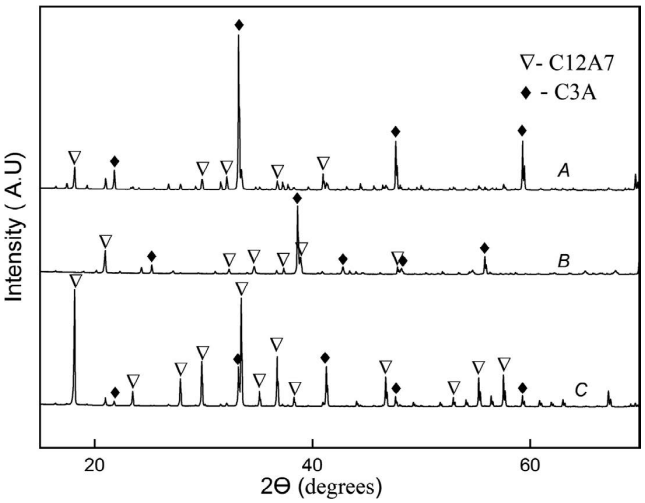

Fig. 1. XRD spectra for the binary of C12A7 and C3A: (A) 20% of C12A7, (B) 40% of C12A7 and (C) 80% of the C12A7 phase fraction.

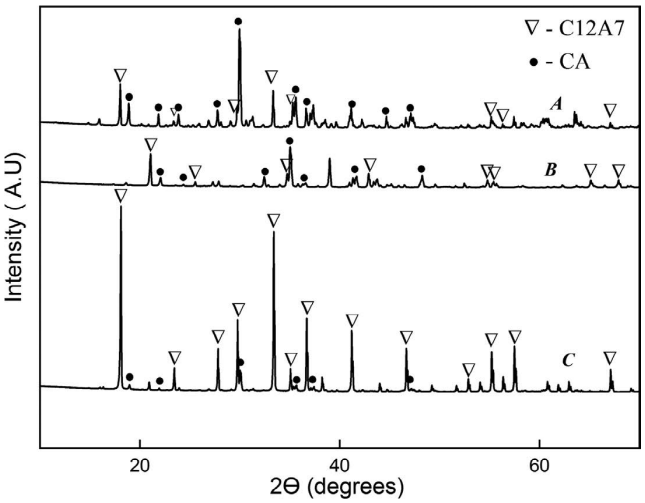

Fig. 2. XRD spectra for the binary of C12A7 and CA: (A) 20% of C12A7, (B) 40% of C12A7 and (C) 80% of the C12A7 phase fraction.

3.2. Analysis of Phase Fractions Based on Raman Spectra

The Raman spectra measured from the binary phase samples of calcium aluminates and the Raman spectra shift (cm^{-1}) for the specified phases (C3A, C12A7 and CA) corresponds with the already published work.[25–29)] The measured sample Raman shifts were within a range of ± 5 cm^{-1} with the ones shown in **Table 3**.

The Raman spectra measured from the samples with binary phases containing C12A7 and C3A show that an increment in the C12A7 phase fraction had a corresponding increase in the peak intensities at the Raman shift region of 510–520 cm^{-1}. This is attributable to C12A7 as a result of its most intense peak located at 517 cm^{-1}, **Fig. 3** illustrates

these phenomena. Similarly, **Fig. 4** shows Raman spectra from the binary phase samples containing C12A7 and CA. It is observable from Fig. 4 that the peak intensities increased at around 510–520 cm^{-1} when the phase fraction of C12A7 in the sample increased, while an increase in CA corresponds with the Raman spectra exhibiting the appearance of a peak shoulder at the 545–549 cm^{-1} region.

The quantitative estimation of the binary phase samples of $CaO–Al_2O_3$ was done by using the relative intensity ratios of the Raman band (shifts) for the XRD measured phase fractions. Raman shifts at 314, 517 and 781 cm^{-1} were used for C12A7, 522, 549, 790 cm^{-1} for CA and 508, 756 cm^{-1} for C3A were used for relative intensity calculations and

Table 1. XRD and XRF analyses for binary calcium aluminates phases of C12A7–C3A.

	XRD analysis (wt%)		Calculated from XRD results (wt%)		XRF analysis (wt%)		Difference between XRD and XRF (wt%)	
Sample	C12A7	C3A	CaO	Al_2O_3	CaO	Al_2O_3	CaO	Al_2O_3
X1	80	20	51.28	48.72	54.01	45.99	2.73	–2.73
X2	74	26	52.10	47.90	54.99	45.01	2.89	–2.89
X3	72	28	52.37	47.63	54.47	45.53	2.10	–2.10
X4	65	35	53.34	46.66	56.21	43.79	2.87	–2.87
X5	61	39	53.89	46.11	56.92	43.08	3.03	–3.03
X6	53	47	54.98	45.02	58.85	41.16	3.86	–3.86
X7	42	58	56.50	43.50	58.82	41.18	2.32	–2.32
X8	40	60	56.77	43.23	59.94	40.06	3.17	–3.17
X9	33	67	57.73	42.27	61.66	38.34	3.93	–3.93
X10	31	69	58.01	41.99	60.96	39.04	2.95	–2.95
X11	27	73	58.56	41.44	61.25	38.75	2.69	–2.69
X12	21	79	59.38	40.62	61.94	38.06	2.56	–2.56

Table 2. XRD and XRF analyses for binary calcium aluminate phases of C12A7–CA.

	XRD analysis (wt%)		Calculated from XRD results (wt%)		XRF analysis (wt%)		Difference between XRD and XRF (wt%)	
Sample	C12A7	CA	CaO	Al_2O_3	CaO	Al_2O_3	CaO	Al_2O_3
Y1	83	17	46.31	53.17	50.01	49.99	3.68	–3.68
Y2	67	33	44.22	55.61	47.53	52.47	3.31	–3.31
Y3	60	40	43.31	57.60	46.96	53.04	3.56	–3.56
Y4	56	44	42.79	55.66	45.89	54.11	3.65	–3.65
Y5	52	48	42.40	57.21	45.96	54.04	3.10	–3.10
Y6	49	51	41.88	58.12	45.07	54.93	3.19	–3.19
Y7	45	55	41.35	58.65	45.52	54.48	4.17	–4.17
Y8	37	63	40.31	59.69	43.70	56.30	3.39	–3.39
Y9	32	68	39.66	60.34	43.00	57.00	3.34	–3.34
Y10	28	72	39.14	60.99	41.45	58.55	2.44	–2.44
Y11	24	76	38.61	60.73	43.14	56.86	4.53	–4.53
Y12	20	80	38.09	61.91	40.31	59.69	2.22	–2.22

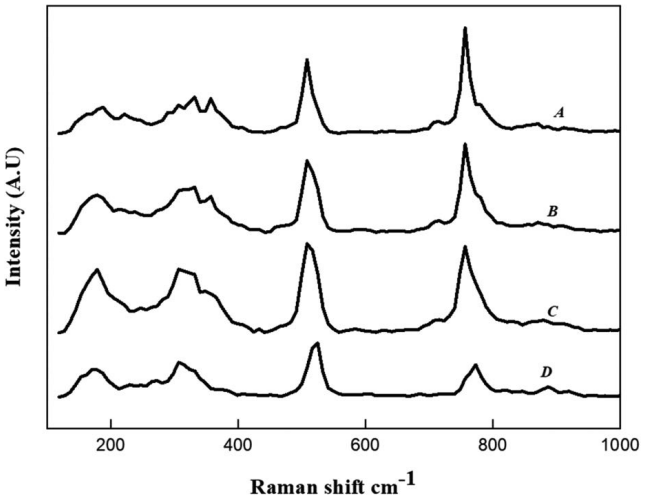

Fig. 3. Raman spectra for the binary C12A7–C3A phase sample: (A) 20% of C12A7, (B) 40% of C12A7 (C) 50% of C12A7 and (D) 80% of the C12A7 phase fraction.

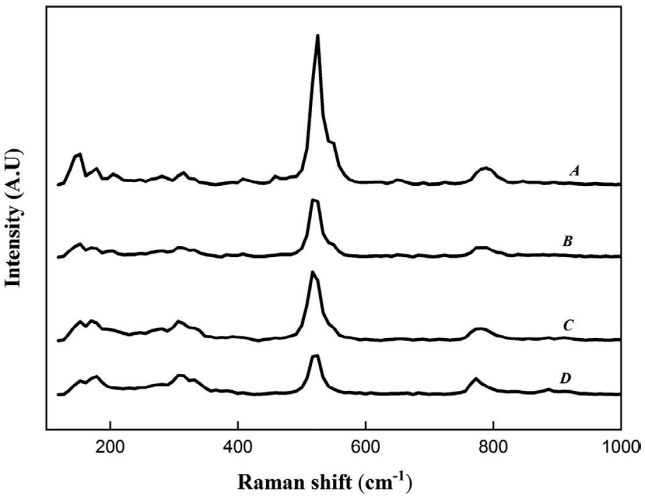

Fig. 4. Raman spectra for the binary C12A7–CA phase sample: (A) 20% of C12A7, (B) 40% of C12A7 (C) 50% of C12A7 and (D) 80% of the C12A7 phase fraction.

Table 3. Reference Raman shift (cm^{-1}) for calcium aluminate phases for this study (s-strong, m-medium and w-weak).

C12A7 [Raman shift (cm^{-1})]		C3A [Raman shift (cm^{-1})]		CA [Raman shift (cm^{-1})]	
Measured	Reference	Measured	Reference	Measured	reference
314 *m*	(312–333) [29] *m*		(140, 150) [27] *w*	522 *s*	(520–521) [26–28] *m*
517 *s*	(516–517) [25,27] *s*	508 *m*	(506–508) [26,27] *m*	549 *m*	(545–547) [26–29] *m*
	772 [29] *m*	756 s	(756 s–757) [26,27,29] *s*	790 *w*	(790–793) [26,27,29] *w*
781 *m*	779 [25] *m*				

analysis. These values were used to estimate a linear regression between the XRD-measured phase fraction and the relative intensity Raman band. Linear regressions were carried out for all the distinct Raman bands associated with the phases in the sample. The analysis of the calibration variable candidates was carried out as presented in Section 2.6. The analysis was conducted separately for both of the considered systems. Equation (1) was used for relative Raman intensity estimation for each of the observed intensity peaks of the studied spectrums.

The linear calibration models between the relative intensities of the Raman band and phase fractions were constructed and evaluated as presented in Section 2.6. The average values of the coefficient of determination and mean absolute error of prediction for 112 random splits for each of the calibration variable candidates are presented in **Table 4**. The most stable calibration variable candidate is the one that has the highest accuracy as well as the highest degree of repeatability, which can be deduced from the small deviation of the normalised calibration parameters between the repetitions. **Figures 5** and **6** illustrate that the error of the calibration, and validation correlates well with the stability of the given variable.

It can be observed from Table 4 that the ratio of the most intense Raman band at 517 cm^{-1} for C12A7 and medium Raman band at 508 cm^{-1} for C3A had the best coefficient of determination values as well as the lowest mean absolute error (MAE). The evaluation of these Raman bands gives a better coefficient of determination and mean absolute error estimation compared to other peaks in Table 4. Figure 5 shows that for C12A7–C3A, the best relative intensity of the Raman Shift ratio for 517/508 performs slightly better than 517/756. Based on the quantitative figures of merit, the most suitable calibration variable for the C12A7-C3A-system is the relative intensity of the peaks at Raman shifts 517 and 508. However, further analysis of the raw spectra reveals that the intensity at shift 517 overlaps with the intensity of the peak at shift 508, which makes the corresponding relative intensity a non-suitable calibration variable due to the saturated intensity values. Additionally, it can be seen that shift 756 represents the decrease of the secondary phase in the binary system with fair accuracy, which can be indicated from the damping of the intensity with respect to the increase in the phase fraction of the primary phase. It can be concluded that the most suitable relative intensity for the prediction of the phase fraction of C12A7 in the C12A7-C3A-system is determined from the maximum intensities at shifts 517 and 756. Therefore, the relative intensity of the Raman Shift ratio of 517/756 is more suitable for quantitative analysis for binary samples of C12A7–C3A. **Figure 7** shows the linear correlation between 517 cm^{-1} and 756 cm^{-1} in the relative intensity and weight percentage phase fraction for C12A7.

Similarly, a calibration line between the relative intensity ratios of the Raman band (shifts) and weight percentage phase fractions for C12A7–CA were made for all the Raman bands for C12A7 and CA. **Table 5** illustrates that the relative intensity ratio of 314 cm^{-1} and 549 cm^{-1} had the highest linear regression fit coefficient of determination (R^2 = 0.97) value compared to others. Furthermore, the mean absolute error for both training and validation data sets were the lowest for an intensity ratio of 314/549. The stability analysis presented in Fig. 6 further confirms that for the C12A7–CA samples, the peak ratio of 314/549 was the best. These Raman bands (C12A7 at 314 cm^{-1} and CA

Table 4. Evaluation of the coefficient of determination and mean absolute error (MAE) of the prediction and validation between the relative intensity of the peaks and the measured phase fraction in the sample (C12A7–C3A).

Phases	Relative intensity	Training data		Validation (ExVal)		Relative Stability
		Mean (R^2)	Mean (MAE)	Mean (R^2)	Mean (MAE)	
C12A7–C3A	517/508	0.97	2.69	0.97	3.04	0.32
C12A7–C3A	517/756	0.96	2.94	0.96	3.31	0.27
C12A7–C3A	314/756	0.94	3.67	0.93	3.78	0.16
C12A7–C3A	314/508	0.92	4.02	0.91	4.26	0.12
C12A7–C3A	781/756	0.91	4.74	0.93	5.22	0.09
C12A7–C3A	781/508	0.83	6.46	0.85	6.87	0.05

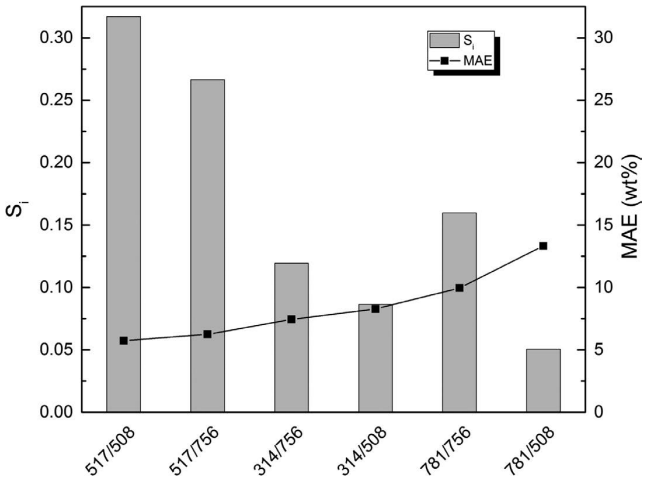

Fig. 5. Relative stabilities of the calibration variable candidates and their corresponding mean absolute error values for training and validation sets (C12A7–C3A).

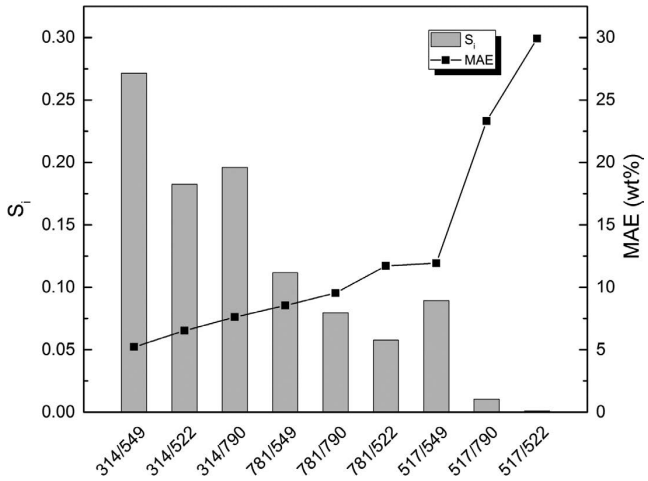

Fig. 6. Relative stabilities of the calibration variable candidates and their corresponding mean absolute error values for training and validation sets (C12A7–CA).

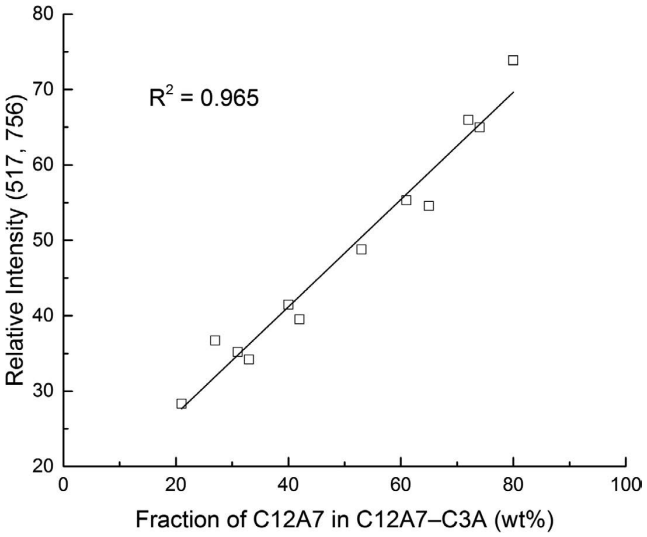

Fig. 7. Raman spectroscopy estimation for the phase fraction for C12A7 as a function of the phase fraction of C12A7 in a calcium-aluminate binary phase (C12A7-C3A).

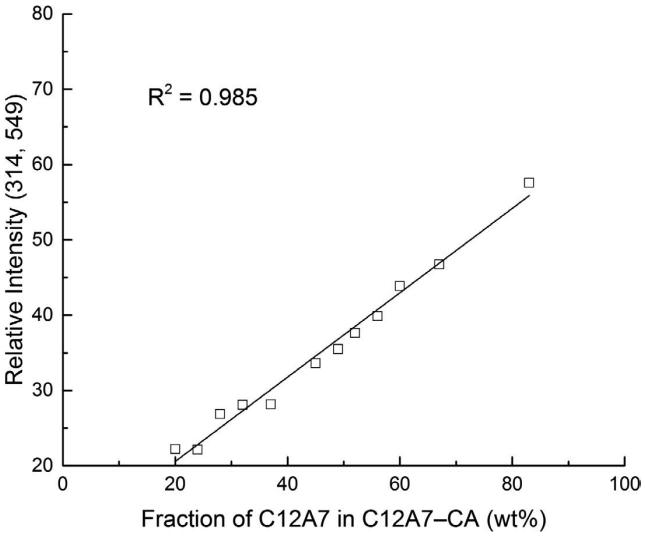

Fig. 8. Raman spectroscopy estimation for the phase fraction of C12A7 as a function of the phase fraction of C12A7 in calcium-aluminate binary phase (C12A7-CA).

Table 5. Evaluation of the coefficient of determination and mean absolute error (MAE) of the prediction and validation between the relative intensity of peaks and the measured phase fraction in the sample (C12A7–CA).

Phases	Relative intensity	Training data		Validation (ExVal)		Relative Stability
		Mean (R^2)	Mean (MAE)	Mean (R^2)	Mean (MAE)	
C12A7–CA	314/549	0.97	2.52	0.97	2.70	0.27
C12A7–CA	781/549	0.95	3.19	0.94	3.34	0.20
C12A7–CA	314/522	0.94	3.69	0.93	3.93	0.18
C12A7–CA	314/790	0.92	4.14	0.90	4.41	0.11
C12A7–CA	517/522	0.88	4.46	0.88	5.09	0.09
C12A7–CA	517/549	0.84	5.64	0.82	6.09	0.08
C12A7–CA	517/790	0.86	5.70	0.87	6.24	0.06
C12A7–CA	781/522	0.45	11.12	0.43	12.20	0.00
C12A7–CA	781/790	0.03	14.41	0.17	15.51	0.01

at 549 cm^{-1}) are far from each other, therefore they will not overlap. The most intense Raman bands for C12A7 at 517 cm^{-1} and CA at 524 cm^{-1} were found to be not very suitable for the analysis. Table 5 demonstrates that the values for the coefficient of determination and mean absolute error for both the training and validation analysis for intense peaks at 517 cm^{-1} and 524 cm^{-1} for C12A7 and CA respectively were not the best. Figure 6 also confirmed that the stability of the relative intensity ratio for 517/524 is not high, as there was a large deviation between the measurement repetitions. The insufficient accuracy of the 517 and 524 cm^{-1} bands are most probably due to them overlapping with each other. The Raman band for C12A7 at 314 cm^{-1} and CA at 549 cm^{-1} are quantitatively the most suitable Raman band for this study. **Figure 8** illustrates an example of a linear correlation between the 314 cm^{-1} and 549 cm^{-1} relative intensity ratio and weight percentage phase fractions for C12A7.

Some deviations from the linear correlation were noticed when there was a high phase fraction difference in the samples. This was most likely due to using XRD as a reference method. The accuracy of XRD is in range of percentages, which will lead to a high precentral error when either of the phase fractions is low. Another explanation could be attributed to a slight instrumental variation, such as the frequency of scattered radiation, or the response of the detection system and incident laser power. Therefore, the intensity of the Raman band could be affected. The variance of error depending on the phase fraction means that the range of phase fraction relevant to the calcium aluminate inclusions analysis needs to be studied in more detail.

3.3. Practical Implications

Figure 9 illustrates the phase diagram for the $CaO–Al_2O_3$ system calculated using the *FactSage*™ computer software to estimate the stability areas for C3A, C12A7 and CA phases. It was also used to show the liquidus region, which can be used to assess the behavior of inclusions under steelmaking temperature. The lowest liquidus temperature can be achieved when the inclusions are close to the C12A7 ($12CaO.7Al_2O_3$) stoichiometric composition with a CaO/Al_2O_3 weight ratio of approximately 0.96. When calcium treatment is conducted in industrial conditions, the difficulty is in defining the correct addition of calcium without knowing the exact composition of the inclusions. When the composition of the inclusions changes from a stoichiometric C12A7 composition, the liquidus temperature increases and CA or C3A phases are formed. Depending on the casting temperature, an increase in the CA or C3A phases can lead to the inclusions becoming solid. For instance, according to Fig. 9, the liquidus temperature of the inclusions exceed the normal casting temperature of 1 520°C when the weight ratio of CaO/Al_2O_3 falls outside the range of 0.75–1.27.

The use of Raman spectroscopic characterisation techniques for oxide inclusions associated with calcium aluminate phases offers an opportunity to estimate whether the inclusions generated fall within the liquidus region. When the Raman spectrum analysis indicates that the weight ratio of CaO/Al_2O_3 in a C12A7–C3A system is above 1.79 ± 0.07, in a normal casting temperature of 1 520°C the cal-

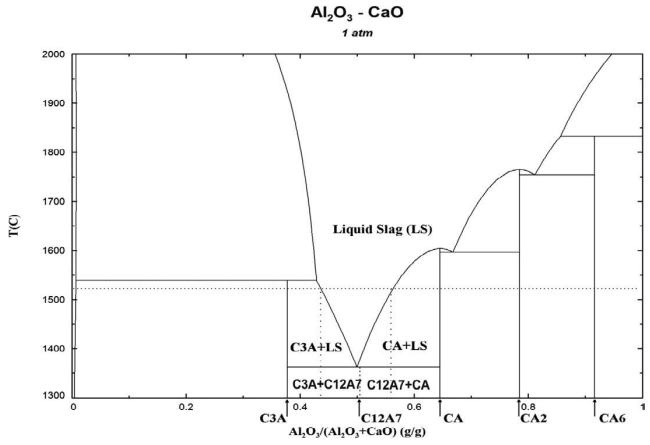

Fig. 9. Phase diagram of the binary $CaO–Al_2O_3$ system.[46]

cium aluminate inclusions would be solid. Similarly, when the Raman measurement indicates that the weight ratio of CaO/Al_2O_3 in a C12A7–CA system is below 1.02 ± 0.04, the calcium aluminate inclusions would be solid in a normal casting temperature of 1 520°C. In this case, more calcium should be added to make the inclusions liquid. The accuracy of the C12A7 to C3A and C12A7 to CA had mean absolute errors of 2.97 and 2.55 percentage points respectively. This means that to obtain liquid inclusions despite the error the weight ratio of CaO/Al_2O_3, obtained from Raman peak ratio values needs to exceed values of 0.98 and be below 1.86 for C12A7–CA and C12A7–C3A respectively.

The obtained results describe the ratio of different calcium aluminates. However, in industrial steel samples there can be $MgO.Al_2O_3$ spinel, or CaS phases in the inclusions. In future work, these phases should be added to Raman spectroscopic characterisation. The accuracy of determining the phase fractions could be potentially increased by utilising a more stable instrument for the reference sample analysis. The accuracy in quantitative Raman spectroscopy could possibly be improved with instrumental parameters with a stable laser power, high resolution and using samples with known properties.

4. Conclusions

This study presents an alternative analytical method for using Raman spectroscopy to carry out qualitative and quantitative analysis to estimate the phase fractions of calcium aluminate phases relevant to steelmaking. The findings of this study can be summarised as follows:

(1) Raman band for C12A7 at 517 cm^{-1} and C3A at 756 cm^{-1} were found to be suitable for quantifying binary C12A7–C3A samples and 314 cm^{-1} for C12A7 and 549 cm^{-1} for CA for quantifying binary C12A7–CA.

(2) The phase fraction of C12A7–C3Aand C12A7–CA could be defined as the mean absolute error of 2.97 and 2.55 percentage points.

(3) The practical implications of the measurement accuracy found in this study in the control of calcium treatment has the potential for estimating inclusions generated within the liquidus window at steelmaking temperatures.

REFERENCES

1) L. Zhang and B. G. Thomas: *Metall. Mater. Trans. B*, **37** (2006), 733.
2) Z. Y. Xu, J. H. Liu, Z. J. He and Q. H. Pang: *Metalurgija*, **57** (2018), 79.
3) L. Zhang and B. G. Thomas: *ISIJ Int.*, **43** (2003), 271.
4) L. Holappa, M. Hämäläinen, M. Liukkonen and M. Lind: *Ironmaking Steelmaking*, **30** (2003), 111.
5) Z. Deng and M. Zhu: *ISIJ Int.*, **54** (2014), 1498.
6) K. Taguchi, H. Ono-Nakazato, T. Usui, K. Marukawa, K. Katogi and H. Kosaka: *ISIJ Int.*, **45** (2005), 1572.
7) K. Rackers and B. G. Thomas: 78th Steelmaking Conf. Proc., Iron and Steel Society, Warrendale, PA, (1995), 723.
8) G.-j. Chen, S.-p. He, Y.-t. Guo, B.-y. Shen, S. Zhao and Q. Wang: *J. Iron Steel Res. Int.*, **22** (2015), 590.
9) T. Lis: *Metalurgija*, **48** (2009), 95.
10) P. C. Pistorius, P. Presoly and K. G. Tshilombo: Sohn Int. Symp. on Advanced Processing of Metals and Materials, Vol. 2, The Minerals, Metals and Materials Society (TMS), Warrendale, (2006), 373.
11) J. C. S. Pires and A. Garcia: *Rem Rev. Esc. Minas*, **57** (2004), 183.
12) S. Abdelaziz, G. Megahed, I. El-Mahallawi and H. Ahmed: *Ironmaking Steelmaking*, **36** (2009), 432.
13) Y. Wang, M. Valdez and S. Sridhar: *Metall. Mater. Trans. B*, **33** (2002), 625.
14) M. Lind and L. Holappa: *Metall. Mater. Trans. B*, **41** (2010), 359.
15) B. G. Bartosiaki, J. A. M. Pereira, W. V. Bielefeldt and A. C. F. Vilela: *J. Mater. Res. Technol.*, **4** (2015), 235.
16) S. Imashuku, K. Ono, R. Shishido, S. Suzuki and K. Wagatsuma: *Mater. Charact.*, **131** (2017), 210.
17) S. Imashuku and K. Wagatsuma: *Metall. Mater. Trans. B*, **49** (2018), 2868.
18) P. Kaushik, H. Pielet and H. Yin: *Ironmaking Steelmaking*, **36** (2009), 561.
19) P. Kaushik, H. Pielet and H. Yin: *Ironmaking Steelmaking*, **36** (2009), 572.
20) N. Noguchi, K. Shinoda and K. Masuda: *J. Mineral. Petrol. Sci.*, **104** (2009), 253.
21) P. Asadena and C. Alifornia: *Appl. Spectrosc.*, **57** (2003), 20A.
22) J. A. Muñoz Tabares and M. J. Anglada: *J. Am. Ceram. Soc.*, **93** (2010), 1790.
23) J. H. Giles, D. A. Gilmore and M. B. Denton: *J. Raman Spectrosc.*, **30** (1999), 767.
24) J. H. Park: *Metall. Mater. Trans. B*, **44** (2013), 938.
25) E. Feizi, J. J. Ojeda and A. K. Ray: *J. Mater. Sci. Mater. Electron.*, **25** (2014), 2261.
26) D. R. Neuville, G. S. Henderson, L. Cormier and D. Massiot: *Am. Mineral.*, **95** (2010), 1580.
27) D. R. Neuville, L. Cormier, A.-M. Flank and D. Massiot: XANES and Raman spectrometry on glasses and crystals in the CAS system, Institut de Physique du Globe de Paris, http://www.ipgp.fr/~neuville/CAS2.pdf. (accessed 2018-01-06).
28) M. Ruszak, S. Witkowski, P. Pietrzyk, A. Kotarba and Z. Sojka: *Funct. Mater. Lett.*, **04** (2011), 183.
29) D. Torréns-Martín, L. Fernández-Carrasco, S. Martínez-Ramírez, J. Ibáñez, L. Artús and L. T. Matschei: *J. Am. Ceram. Soc.*, **96** (2013), 3589.
30) S. Li and L. H. Hihara: *J. Raman Spectrosc.*, **48** (2017), 137.
31) C. A. Cooper, R. Elliott and R. J. Young: *J. Mater. Sci.*, **38** (2003), 795.
32) C. Hirlimann, M. Jouanne and C. Forriès: *J. Raman Spectrosc.*, **23** (1992), 315.
33) J. R. Ferraro, K. Nakamoto and C. W. Brown: Introductory Raman Spectroscopy, 2nd ed., Elsevier, Cambridge, (2003), 1.
34) Z. Wang, Q. Shu and K. Chou: *ISIJ Int.*, **51** (2011), 1021.
35) K. Zheng, J. Liao, X. Wang and Z. Zhang: *J. Non-Cryst. Solids*, **376** (2013), 209.
36) Y. Zhen, G. Zhang and K. Chou: *ISIJ Int.*, **54** (2014), 985.
37) W. Huang, Y. Zhao, S. Yu, L.-x. Zhang, Z.-c. Ye, N. Wang and M. Chen: *ISIJ Int.*, **56** (2016), 594.
38) H. Park, J. Y. Park, G. H. Kim and I. Sohn: *Steel Res. Int.*, **83** (2012), 150.
39) J. H. Park: *ISIJ Int.*, **52** (2012), 1627.
40) X. Shen, M. Chen, N. Wang and D. Wang: *ISIJ Int.*, **59** (2019), 9.
41) C. Feng, J. Tang, L. Gao, Z. Liu and M. Chu: *ISIJ Int.*, **59** (2019), 31.
42) T. Lipiäinen, J. Pessi, P. Movahedi, J. Koivistoinen, L. Kurki, M. Tenhunen, J. Yliruusi, A. M. Juppo, J. Heikkonen, T. Pahikkala and C. J. Strachan: *Anal. Chem.*, **90** (2018), 4832.
43) F. Harrell: Regression Modeling Strategies, Springer, New York, (2001), 568.
44) K. Baumann: *Trends Anal. Chem.*, **22** (2003), 395.
45) K. Baumann and N. Stiefl: *J. Comput. Aided Mol. Des.*, **18** (2004), 549.
46) C. W. Bale, E. Bélisle, P. Chartrand, S. A. Decterov, G. Eriksson, K. Hack, K. Hack, I.-H. Jung, Y.-B. Kang, J. Melançon, A. D. Pelton, C. Robelin and S. Petersen: *Calphad*, **33** (2009), 295.